RSC Advances

PAPER

View Article Online
View Journal | View Issue

Cite this: *RSC Adv.*, 2023, **13**, 23038

A single step wet chemical approach to bifunctional ultrathin $(ZnO)_{62}(Fe_2O_3)_{38}$ dendritic nanosheets†

Saba Latif,[a] Bilal Akram,[*b] Chaudry Sajed Saraj,[cd] Bilal Ahmad Khan,[*a] Mudussar Ali[e] and Javeed Akhtar[f]

At the ultrathin scale, nanomaterials exhibit interesting chemical and physical properties, like flexibility, and polymer-like rheology. However, to limit the dimensions of composite nanomaterials at the ultrathin level is still a challenging task. Herein, by adopting a new low temperature single step and single pot wet chemical approach, we have successfully fabricated two dimensional (2D) mixed oxide $ZnO–Fe_2O_3$ dendritic nanosheets (FZDNSs). Various control experimental outcomes demonstrate that precursor salts of both the metals are crucial for the formation of stable 2D FZDNSs. The obtained FZDNSs not only exhibit the best photoreduction performance but also much enhanced electrocatalytic performance. This work will provide a promising avenue for the synthesis of cost effective transition metal mixed oxide based 2D nanosheets having wide ranging applications.

Received 17th July 2023
Accepted 25th July 2023

DOI: 10.1039/d3ra04795d

rsc.li/rsc-advances

Currently, ultrathin two dimensional (2D) nanosheets are attracting considerable attention[1–5] because of their characteristic features and broad range of applications in the fields of catalysis,[3,5] optics,[6,7] energy[4,8] and sensing,[9,10] *etc.* Among various 2D materials, the mixed oxide based ultrathin 2D nanosheets developed from two different materials usually exhibit superior properties in various applications, that might be because of the synergy of different components.[4] For example, the 2D ultrathin nanosheets obtained from different components have shown superior performance in lithium ion batteries,[11] solar cells[12] and photocatalysis.[13]

Numerous strategies are in practice to obtain nanosheets, like mechanical exfoliation,[14] electrochemical Li-intercalation and exfoliation,[15] direct sonication in solvents,[16,17] solution based synthesis[18,19] and chemical vapor deposition (CVD),[20,21] *etc.* However, most of the aforementioned routes to composite nanosheets require time consuming multi-step processing, lack compositional uniformity and are still challenging to limit the thickness at ultrathin level.

Besides these approaches, there are number of reports about the wet chemical synthesis of nanosheets.[22–25] However, all these solutions based chemical synthetic routes involve the use of long chain surfactants like oleic acid or oleylamine *etc.* All these strategies lead to the formation of nanosheets but their surface remains capped with that insulating surfactants or ligands which hinder their performance towards most of the applications. Therefore, it is still challenging to develop a surfactant free easy approach to fabricate nanosheets of two different materials.

The wide range applications of transition metal oxides has inspired an immense interest to comprehend and tailor their properties in order to get improved functionalities.[26–30] For instance, the hybrid materials obtained from iron and cobalt act as unique soft magnetic material due to their novel magnetic characteristics such as large permeability and much higher saturation magnetization. In another report, iron cobalt mixed oxides laminar structures have been developed having improved multifunctional properties.[31] The fabrication of ultrathin 2D nanosheets having lateral size ranging from several tens of nanometers to micrometers of transition metals based mixed oxides behave as an ideal 2D building block to fabricate advanced functional materials.[23] However there are only few reports exist about the synthesis of transition metal based mixed oxides nanosheets. Yamauchi *et al.* reported the fabrication of two-dimensional mesoporous mixed oxide nanosheets, such as metal cobaltites *via* self-deconstruction/reconstruction of highly uniform Co-based metal glycerate nanospheres using a multistep approach.[32] In another report, Zhang *et al.* adopted a high temperature thermal decomposition approach to obtain Mn–Cr mixed oxides nanosheets that manifest excellent electrochemical performance towards Li

[a]*Department of Chemistry, University of Azad Jammu & Kashmir, Muzaffarabad, AJ&K, Pakistan. E-mail: bkhan@ajku.edu.pk*

[b]*Department of Chemistry, Women University of Azad Jammu & Kashmir, Bagh, AJ&K, Pakistan. E-mail: bai-l16@tsinghua.org.cn*

[c]*GPL, State Key Lab. of Applied Optics, Changchun Institute of Optics, Fine Mechanics and Physics, Chinese Academy of Sciences, Changchun 130033, China*

[d]*University of Chinese Academy of Sciences, Beijing 100049, China*

[e]*Department of Chemistry, Tsinghua University, Beijing, China*

[f]*Materials Lab, Department of Chemistry, Mirpur University of Science and Technology, Mirpur, AJ&K, Pakistan*

† Electronic supplementary information (ESI) available. See DOI: https://doi.org/10.1039/d3ra04795d

storage.[33] In another work, Jian-Wen Shi successfully fabricated $H_2Ti_3O_7$ nanowires supported Mn–Co mixed oxide ultrathin nanosheets with enhanced catalytic activities.[34]

Among various 2D transition metal based mixed oxides systems, ZnO based mixed oxide attracted special attention because of defective structure of ZnO. Intrinsic point defects exist in ZnO that heavily affect its various properties. Intrinsic defects lead to the modification of the electronic structure and the valence state of the ions in the matrix.[35] Several researchers have contributed to the current knowledge of intrinsic point defects in bulk ZnO both computationally and experimentally. It is observed that small concentrations of intrinsic defects in ZnO (even 0.01 ppm) modify its electrical and optical properties.[35,36] Moreover 2D nanosheets composed of iron and zinc are the most fascinating materials as they exhibit superior photocatalytic performance because of their intrinsic surface plasmon resonance (SPR)[37,38] properties. Moreover, when such materials are confined to ultrathin level, their surface will become saturated with more electrons and active centers that leads to an enhancement in their overall catalytic performance. Due to the synergistic effect, iron and zinc based mixed oxides is supposed to have even superior performance towards catalytic, optical and energy related applications. Core–shell Fe_2O_3/ZnO nanosheets have been synthesized hydrothermally that can act as efficient bactericide cum photocatalyst for environmental remediation.[39] Fe–Zn based mixed oxides porous nanosheets have been developed using solvothermal approach which show promising performance towards photooxidation of methane to methanol.[24] The aforementioned reports suggested that the transition metal based mixed oxides nanosheets are very important materials for a variety of applications, but their synthesis is still not an easy task.

Herein, by adopting a surfactant/ligand free solution-based strategy, we have achieved the controllable synthesis of the 2D hybrid ZnO–Fe_2O_3 DNSs by adding both precursors within the reaction system *via* one step low temperature solution-based approach. Furthermore, owing to the combinatorial effect of Fe_2O_3 and ZnO, the obtained DNSs showed enhanced photocatalytic as well as electrocatalytic activity.

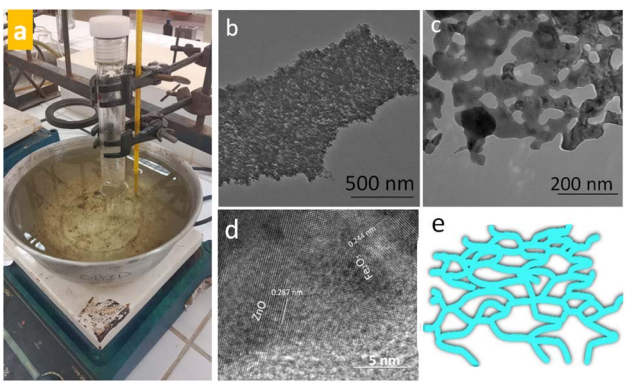

Fig. 1 (a) Digital photograph of experimental set up (b and c) TEM images of obtained FZDNSs at different magnifications (d) HRTEM image of FZDNSs and (e) schematic of FZDNSs.

Surfactants/ligands free low temperature wet chemical approach (Fig. 1a) was adopted to obtain FeZn mixed oxides dendritic nanosheets (FZDNSs). The electron microscopy analysis reveals the structural features of obtained test analytes. Fig. 1b and c reveals the transmission electron microscopy (TEM) images of obtained mixed oxides nanosheets. The obtained nanosheets are single layer with thickness of few nanometers having network structure. More importantly, HRTEM images revealed in Fig. 1d indicate the existence of two different structural domains, one of which have an interlayer spacing of 0.287 nm referring to the (100) and (010) planes of ZnO. Whereas, the other having spacing of 0.244 nm correspond to the (400) and (040) planes of Fe_2O_3. These results confirmed the formation of mixed structure. Fig. 1e indicate the schematic of dendritic nanosheets. The product purity is revealed by scanning electron microscopy image (Fig. S1†). The SEM image reveals several free standing nanosheets with no other detectable morphology.

The pure ZnO has irregular shaped particles of different sizes as indicated through TEM image shown in Fig. S2a.† Similarly, pure Fe_2O_3 has irregular morphology containing few sheets and rod like structures as shown in Fig. S2b.† The above findings signifies that the precursors salts of both the metals have substantial influence in determining the structure of final mixed oxide product.

The compositional analysis of obtained dendritic nanosheets has been investigated through powder X-ray diffraction (XRD). The XRD pattern revealed in Fig. 2a shows the presence of characteristic peaks of both the ZnO and Fe_2O_3 which can be indexed well with the standard pattern of ZnO and Fe_2O_3. The appearance of sharp peaks in the XRD pattern indicate their well crystalline nature. The composition of the obtained FZDNSs was further inveterate using energy dispersive X-ray spectroscopy (EDX). The EDX spectrum (Fig. 2b) shows that the obtained dendritic nanosheets are well composed of both iron oxide and zinc oxide components. Few additional peaks in the EDX spectrum refers to the presence of impurities from the substrate. The precise elemental ratio and hence molecular formula of the obtained nanosheets was estimated using ICP-OES analysis (Table S1†) and it comes out to be $(ZnO)_{62}(Fe_2O_3)_{38}$.

FTIR spectra of FZDNSs (Fig. 3a) shows two bands in the 700–500 cm^{-1} region which evidenced the formation of mixed metal oxides and are in well agreement with reported literature.[31,40] Thermal stability of the FZDNSs was investigated through thermogravimetric analysis (TGA) (Fig. 3b), and no significant weight loss was observed. The observable weight loss

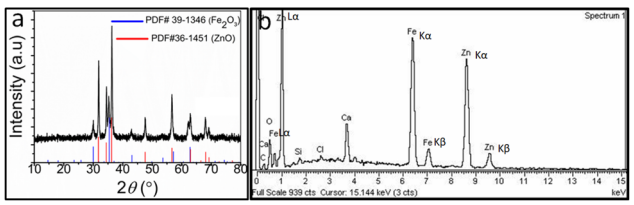

Fig. 2 (a) XRD pattern (b) EDX spectrum of FZDNSs.

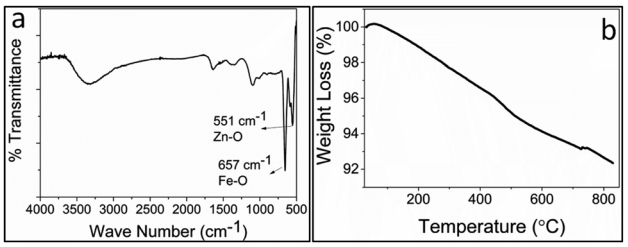

Fig. 3 (a) FTIR spectrum and (b) TGA of FZDNSs.

may be attributed to the removal of solvents and adsorbed water. The overall result of TGA analysis indicate the better thermal stability of the obtained nanosheets.

The optical features of the FZDNSs were estimated using ultraviolet-visible (UV-vis) spectroscopy (Fig. 4a). FZDNSs show a wide range of absorption bands in the visible region. The broad range absorption can be further complemented through brown appearance and ultrathin nature (Fig. 4a). As the thickness approaches to few nanometers scale, the materials show quantum confinement effect which leads to the absorption in the visible region (red shift). Benefiting from the wide absorption features, the obtained FZDNSs were potentially employed as photocatalysts by taking conversion of *para* nitrophenol to *para*-aminophenol as a model reaction. This conversion is of practical utility since *p*-nitrophenol (the reactant) is highly toxic and *p*-aminophenol (the product) is of significant industrial importance.[41]

The performance of photocatalysts towards *p*-nitrophenol reduction was conducted under visible light illumination employing sodium borohydride as reducing agent. As indicated in Fig. 4b, aqueous solution of PNP shows an absorption peak centered around 400 nm. With the presence of the FZDNSs catalyst and visible light illumination, the characteristic peak of *p*-nitrophenol gradually decreases. Meanwhile, a new absorption peak centered around 300 nm appears which correspond to *p*-aminophenol. This peak gradually increases in height with the passage of time. *p*-Nitrophenol is very stable and conversion was not being observed in the absence of FZDNSs catalyst and $NaBH_4$. The control experiment reveals that all the factors (catalyst, $NaBH_4$ and light illumination) are necessary for the efficient *p*-nitrophenol reduction.

The conversion ratio of *p*-nitrophenol using pure ZnO and Fe_2O_3 is also presented in Fig. 4c which indicates the much-enhanced comparative performance of mixed oxides. More importantly, the photoreduction performance of the FZDNSs were higher than those of previously reported photocatalysts as indicated in Table S2,† further confirming the superiority of the construction of heterostructure. Oxides of iron attracted special attention due to its high absorptive supremacy in the visible window.[42] However, its practical utility towards photocatalytic applications is limited due to the narrow band energy gap ($\leq$2.2) and exciton recombination.[43] These issues can be well overcome through compositing, quantum confinement or architectural modifications. Band gap of ZnO is relatively wider (3.1 eV) which makes it transparent to the visible region of the spectrum.[43] To our delight, the combination of ZnO with Fe_2O_3 has been used to obtain a new structure with improved properties that individual oxide doesn't possess as indicated by our results. The improved performance of FZDNSs can be credited to the synergistic effect of both iron and zinc as well as the unique 2D structure. The FZDNSs are catalytically stable and can be reused for four duplicate operations as indicated in Fig. 4d.

The electrocatalytic HER performance of each catalyst was firstly evaluated using a three-electrode system in basic environment. The ZnO/CC, Fe_2O_3/CC, FZDNSs/CC and Pt wire were also measured as contrast under the same conditions. FZDNSs shows much enhanced HER performance as compared to pure ZnO and Fe_2O_3. The overpotentials of HER on FZDNSs/CC at current density of 10 mA cm^{-2} and 50 mA cm^{-2} are only 182 mV and 377 mV, respectively, which are much lower than those of ZnO/CC (η_{10} = 647 mV, η_{40} = 788 mV) and Fe_2O_3/CC (η_{10} =

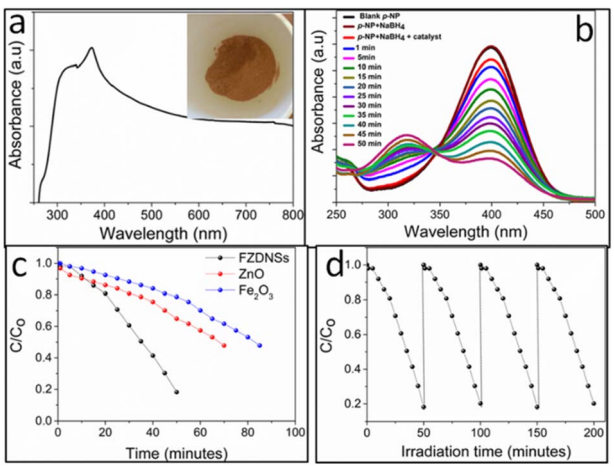

Fig. 4 (a) UV-vis spectrum of FZDNSs (inset is the digital photograph of FZDNSs) (b) UV vis spectrum revealing successive photoconversion of *p*-nitrophenol to *p*-aminophenol, (c) comparative photocatalytic performance of pure and mixed oxides and (d) catalyst (FZDNSs) stability test.

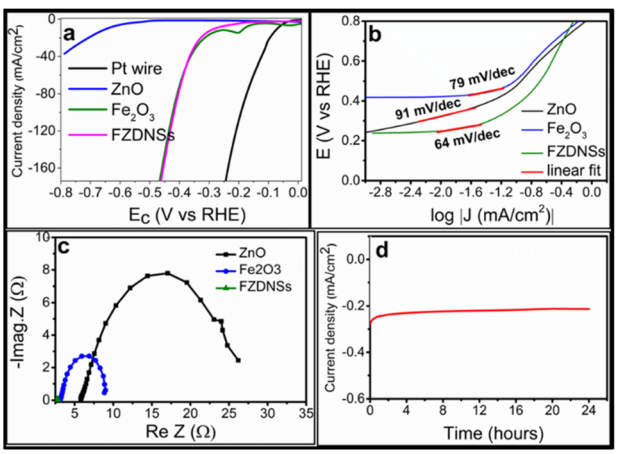

Fig. 5 HER performance (a) polarization curves, (b) corresponding Tafel slope, (c) corresponding Nyquist plots of various test analytes, (d) chronoamperometry (CA) test of FZDNSs.

281 mV, η_{50} = 378 mV) as revealed in Fig. 5a. The superior performance of FZDNSs/CC at large current density is credited to the unique 2D nanosheet like structures as well as synergy of both ZnO and Fe_2O_3. These experimental outcomes suggest that FZDNSs/CC reported in this work is one of the best non-precious transition metal-based HER electrocatalyst as indicated in Table S3.†

Compared with the Tafel slopes of ZnO/CC (91 mV dec^{-1}) and Fe_2O_3/CC (79 mV dec^{-1}), the FZDNSs/CC have the least Tafel slope value of 64 mV dec^{-1} which refers to much improved HER kinetic (Fig. 5b). The Tafel slope of the FZDNSs/CC falls in the range of 40–120 mV dec^{-1}, indicating that the HER might proceed *via* Volmer–Heyrovsky mechanism.[44,45] The above finding of Tafel slope suggest that the FZDNSs/CC electrode has highest intrinsic activity towards HER, benefiting from the raising electrons transfer and redistribution induced by mixing of two different oxides.

Fig. 5c shows the electrochemical impedance spectroscopy (EIS) results of various test analytes. The charge transfer resistance (R_{ct}) of each analyte deposited CC electrode are fitted through Z view software. The FZDNSs/CC electrode reveals the R_{ct} of 2.8 Ω which is significantly lower than those of Fe_2O_3/CC (8.9 Ω) and ZnO/CC (26.2 Ω). The lower R_{ct} suggests the high electronic conductivity of FZDNSs/CC which can leads to an improvement in overall electrocatalytic performance.

Furthermore, the stability of an electrocatalyst is another very important factor to be consider while evaluating its overall electrocatalytic performance. The chronopotentiometry curve in Fig. 5d reveals almost constant overpotential, a very small variation in the potential ($\Delta V \sim 4$ mV) is recorded after 24 hours. Moreover, the LSV curve of FZDNSs/CC after chronopotentiometry curve (Fig. S3†) has no obvious change from the corresponding initial curve. These outcomes signify an excellent electrochemical stability of the FZDNSs/CC in an alkaline media.

Generally, the electrochemically active surface area (ECSA) and the activity of the electrocatalysts have direct relationship and can be assessed through electrochemical double-layer capacitances (C_{dl}).[46] The CV tests were carried out at different scan rates to measure the C_{dl} values of the FZDNSs/CC electrode as revealed in Fig. S4.† The C_{dl} value of FZDNSs/CC is 134.28 mF cm^{-2} which is much higher than that of pure oxides. The large C_{dl} value is attributed to the unique ultrathin 2D nature of FZDNSs/CC indicating that it possesses abundant catalytic active sites.

In summary, we have developed a low temperature single step single pot route to unique mixed oxides dendritic nanosheets. The obtained nanosheets were found to be bifunctional and can be used as photocatalyst as well as best electrocatalyst. Such an easy approach to nanosheets can be extended to several other multifunctional complex systems in future.

Conflicts of interest

The authors declare no competing financial interest.

Notes and references

1 L. Liu and X. Chen, *Chem. Rev.*, 2014, **114**, 9890–9918.
2 C. Lin, X. Zhu, J. Feng, C. Wu, S. Hu, J. Peng, Y. Guo, L. Peng, J. Zhao, J. Huang, J. Yang and Y. Xie, *J. Am. Chem. Soc.*, 2013, **135**, 5144–5151.
3 Y. Liu, H. Cheng, M. Lyu, S. Fan, Q. Liu, W. Zhang, Y. Zhi, C. Wang, C. Xiao, S. Wei, B. Ye and Y. Xie, *J. Am. Chem. Soc.*, 2014, **136**, 15670–15675.
4 C. Tan, L. Zhao, P. Yu, Y. Huang, B. Chen, Z. Lai, X. Qi, M. H. Goh, X. Zhang, S. Han, X. J. Wu, Z. Liu, Y. Zhao and H. Zhang, *Angew. Chem.*, 2017, **56**, 7842–7846.
5 N. Yang, Z. Zhang, B. Chen, Y. Huang, J. Chen, Z. Lai, Y. Chen, M. Sindoro, A. L. Wang, H. Cheng, Z. Fan, X. Liu, B. Li, Y. Zong, L. Gu and H. Zhang, *Adv. Mater.*, 2017, **29**, 1700769.
6 S. Yang, W. Niu, A. L. Wang, Z. Fan, B. Chen, C. Tan, Q. Lu and H. Zhang, *Angew. Chem.*, 2017, **56**, 4252–4255.
7 X. Fang, P. Wei, L. Wang, X. Wang, B. Chen, Q. He, Q. Yue, J. Zhang, W. Zhao, J. Wang, G. Lu, H. Zhang, W. Huang, X. Huang and H. Li, *ACS Appl. Mater. Interfaces*, 2018, **10**, 13011–13018.
8 H. Zhu, Z. Lai, Y. Fang, X. Zhen, C. Tan, X. Qi, D. Ding, P. Chen, H. Zhang and K. Pu, *Small*, 2017, **13**, 1604139.
9 A. G. Kenry, A. Geldert, Z. Lai, Y. Huang, P. Yu, C. Tan, Z. Liu, H. Zhang and C. T. Lim, *Small*, 2017, **13**, 1601925.
10 J. Ping, Z. Fan, M. Sindoro, Y. Ying and H. Zhang, *Adv. Funct. Mater.*, 2017, **27**, 1605817.
11 Y. Chen, B. Song, X. Tang, L. Lu and J. Xue, *Small*, 2014, **10**, 1536–1543.
12 J. M. Yun, Y. J. Noh, C. H. Lee, S. I. Na, S. Lee, S. M. Jo, H. I. Joh and D. Y. Kim, *Small*, 2014, **10**, 2319–2324.
13 L. Yang, X. Zhu, S. Xiong, X. Wu, Y. Shan and P. K. Chu, *ACS Appl. Mater. Interfaces*, 2016, **8**, 13966–13972.
14 K. S. Novoselov, D. Jiang, F. Schedin, T. J. Booth, V. V. Khotkevich, S. V. Morozov and A. K. Geim, *Proc. Natl. Acad. Sci. U. S. A.*, 2005, **102**, 10451–10453.
15 Z. Zeng, Z. Yin, X. Huang, H. Li, Q. He, G. Lu, F. Boey and H. Zhang, *Angew. Chem.*, 2011, **50**, 11093–11097.
16 K. G. Zhou, N. N. Mao, H. X. Wang, Y. Peng and H. L. Zhang, *Angew. Chem.*, 2011, **50**, 10839–10842.
17 J. N. Coleman, M. Lotya, A. O'Neill, S. D. Bergin, P. J. King, U. Khan, K. Young, A. Gaucher, S. De, R. J. Smith, I. V. Shvets, S. K. Arora, G. Stanton, H. Y. Kim, K. Lee, G. T. Kim, G. S. Duesberg, T. Hallam, J. J. Boland, J. J. Wang, J. F. Donegan, J. C. Grunlan, G. Moriarty, A. Shmeliov, R. J. Nicholls, J. M. Perkins, E. M. Grieveson, K. Theuwissen, D. W. McComb, P. D. Nellist and V. Nicolosi, *Science*, 2011, **331**, 568–571.
18 H. Zhang, B. H. Savitzky, J. Yang, J. T. Newman, K. A. Perez, B.-R. Hyun, L. F. Kourkoutis, T. Hanrath and F. W. Wise, *Chem. Mater.*, 2015, **28**, 127–134.
19 Y. Wu, B. Yuan, M. Li, W. H. Zhang, Y. Liu and C. Li, *Chem. Sci.*, 2015, **6**, 1873–1878.
20 Y. Shi, W. Zhou, A. Y. Lu, W. Fang, Y. H. Lee, A. L. Hsu, S. M. Kim, K. K. Kim, H. Y. Yang, L. J. Li, J. C. Idrobo and J. Kong, *Nano Lett.*, 2012, **12**, 2784–2791.
21 K. K. Liu, W. Zhang, Y. H. Lee, Y. C. Lin, M. T. Chang, C. Y. Su, C. S. Chang, H. Li, Y. Shi, H. Zhang, C. S. Lai and L. J. Li, *Nano Lett.*, 2012, **12**, 1538–1544.

22 B. Akram, W. Shi, H. Zhang, S. Ullah, M. Khurram and X. Wang, *Angew. Chem.*, 2020, **132**, 8575–8579.
23 F. Zhao, L. Zheng, Q. Yuan, X. Yang, Q. Zhang, H. Xu, Y. Guo, S. Yang, Z. Zhou and L. Gu, *Adv. Mater.*, 2021, **33**, 2103383.
24 K. Zheng, Y. Wu, J. Zhu, M. Wu, X. Jiao, L. Li, S. Wang, M. Fan, J. Hu and W. Yan, *J. Am. Chem. Soc.*, 2022, **144**, 12357–12366.
25 B. Akram, B. Ni and X. Wang, *Adv. Mater.*, 2020, **32**, 1906794.
26 C. Yuan, H. B. Wu, Y. Xie and X. W. Lou, *Angew. Chem., Int. Ed.*, 2014, **53**, 1488–1504.
27 F. Wu, J. Bai, J. Feng and S. Xiong, *Nanoscale*, 2015, **7**, 17211–17230.
28 S. K. Sarkar, S. Ahlawat, S. D. Kaushik, P. Babu, D. Sen, D. Honecker and A. Biswas, *J. Phys.: Condens. Matter*, 2019, **32**, 115801.
29 A. U. Ammar, I. D. Yildirim, F. Bakan and E. Erdem, *Beilstein J. Nanotechnol.*, 2021, **12**, 49–57.
30 M. Buldu-Akturk, M. Toufani, A. Tufani and E. Erdem, *Nanoscale*, 2022, **14**, 3269–3278.
31 N. Kanwal, B. Akram, C. S. Saraj, K. Ahmad, S. H. Talib and H. M. Asif, *New J. Chem.*, 2022, **46**, 9762–9766.
32 Y. V. Kaneti, R. R. Salunkhe, N. L. W. Septiani, C. Young, X. Jiang, Y.-B. He, Y.-M. Kang, Y. Sugahara and Y. Yamauchi, *J. Mater. Chem. A*, 2018, **6**, 5971–5983.
33 L. Li, L. Wang, M. Zhang and Q. Huang, *RSC Adv.*, 2018, **8**, 29670–29677.
34 J. W. Shi, Z. Fan, C. Gao, G. Gao, B. Wang, Y. Wang, C. He and C. Niu, *ChemCatChem*, 2018, **10**, 2833–2844.
35 S. Nadupalli, S. Repp, S. Weber and E. Erdem, *Nanoscale*, 2021, **13**, 9160–9171.
36 S. Najib, F. Bakan, N. Abdullayeva, R. Bahariqushchi, S. Kasap, G. Franzò, M. Sankir, N. D. Sankir, S. Mirabella and E. Erdem, *Nanoscale*, 2020, **12**, 16162–16172.
37 K. Lee, W. S. Seo and J. T. Park, *J. Am. Chem. Soc.*, 2003, **125**, 3408–3409.
38 M. Açıkgöz, M. D. Drahus, A. Ozarowski, J. Van Tol, S. Weber and E. Erdem, *J. Phys.: Condens. Matter*, 2014, **26**, 155803.
39 C. Karunakaran and P. Vinayagamoorthy, *Catal. Today*, 2017, **284**, 114–120.
40 S. G. Christoskova, M. Stoyanova and M. Georgieva, *Appl. Catal., A*, 2001, **208**, 235–242.
41 J. Qian, A. Yuan, C. Yao, J. Liu, B. Li, F. Xi and X. Dong, *ChemCatChem*, 2018, **10**, 4747–4754.
42 P. M. Ganje, H. A. Bandal and K. Hern, *Sustainable Energy Fuels*, 2022, **6**, 5579–5590.
43 G. K. Pradhan, S. Martha and K. Parida, *ACS Appl. Mater. Interfaces*, 2012, **4**, 707–713.
44 C. Wu, Y. Yang, D. Dong, Y. Zhang and J. Li, *Small*, 2017, **13**, 1602873.
45 Y. Yin, C. Xu, Z. Liu, W. Ren and C. Sun, *Int. J. Hydrogen Energy*, 2019, **44**, 853–859.
46 S. Czioska, J. Wang, X. Teng, S. Zuo, S. Xie and Z. Chen, *Nanoscale*, 2018, **10**, 2887–2893.